All-microwave Lamb shift engineering for a fixed frequency multi-level superconducting qubit

Ann, Byoung-Moo; Steele, Gary A.

DOI
10.1038/s42005-024-01841-0

Publication date
2024

Document Version
Final published version

Published in
Communications Physics

communications physics

Article

https://doi.org/10.1038/s42005-024-01841-0

All-microwave Lamb shift engineering for a fixed frequency multi-level superconducting qubit

Check for updates

Byoung-moo Ann [1,2] & Gary A. Steele [1]

It is known that the electromagnetic vacuum is responsible for the Lamb shift, which is a crucial phenomenon in quantum electrodynamics (QED). In circuit QED, the readout or bus resonators that are dispersively coupled can result in a significant Lamb shift of the qubit. However, previous approaches or proposals for controlling the Lamb shift in circuit QED demand overheads in circuit designs or non-perturbative renormalization of the system's eigenbases, which can impose formidable limitations. In this work, we propose and demonstrate an all-microwave method for controlling the Lamb shift of fixed-frequency transmons. We employ the drive-induced longitudinal coupling between the transmon and resonator. By simply using an off-resonant monochromatic drive near the resonator frequency, we can control the net Lamb shift up to ±30 MHz and engineer it to zero with the drive-induced longitudinal coupling without facing the aforementioned challenges. Our work establishes an efficient way of engineering the fundamental effects of the electromagnetic vacuum and provides greater flexibility in non-parametric frequency controls of multilevel systems.

The rise of modern quantum electrodynamics (QED) was motivated by the need to comprehend the effects of vacuum[1,2]. One representative phenomenon that accompanied the development of QED is the Lamb shift, which refers to the renormalization of energy levels induced by the electromagnetic fluctuations of the vacuum. Originally, the Lamb shift concerned systems placed in free space. However, the advent of cavity and circuit-QED[3–5] inspired studies of engineered vacuum. In particular, in circuit-QED, qubits are almost always accompanied by microwave modes in the strong dispersive regime, and Lamb shifts induced by these resonators take significant portions of the bare transition frequency of the qubits[6–12].

Thus, controlling the Lamb shift could provide more flexibility in engineering the transition frequencies of superconducting qubits. In circuit-QED, however, Lamb shift control requires daunting overheads such as flux-tunability[6–9], voltage biasing[13], or collective states[14]. Lamb shift can also be controlled without the aforementioned costs using external drivings, as proposed in[15–17]. Unfortunately, one cannot avoid mixing among the eigenstates in this manner. Consequently, the properties of the systems will undergo unwanted renormalization[18,19].

In this work, we propose and demonstrate an all-microwave approach for Lamb shift control in a typical circuit-QED configuration comprising a transmon[20] dispersively coupled to a single resonator mode. We introduce strong drive fields off-resonant to both the transmon and resonator, inducing drive-induced longitudinal coupling (DLC).

This results in state-dependent frequency shifts of the transmon which exist only when the resonator mode is dispersively coupled and therefore can be used to control the Lamb-shift, representing the core-principle of our Lamb shift engineering scheme. We demonstrate large tuning of the Lamb shift ~30 MHz while minimizing undesired renormalization of the other properties of the transmon-resonator system.

Results

Theoretical descriptions

For a dispersively coupled transmon and resonator system, the renormalized interaction in the strong drive limit has been experimentally verified in our previous work[18]. Unfortuately, the renormalized interaction significantly changes not only the Lamb shift of the transmon, but also other properties such as lifetime, Rabi frequency, and cross-nonlinearity. In this work, we substantially engineer the Lamb shift while avoiding these unwanted renormalization, which was not dealt with in[18].

Figure 1 (a) describes an experimental configuration used in this work. We consider a dispersively coupled transmon and resonator. The drive is

[1]Kavli Institute of Nanoscience, Delft University of Technology, Delft, The Netherlands. [2]Quantum Technology Institute, Korea Research Institute of Standards and Science, Daejeon, South Korea. e-mail: byoungmoo.ann@gmail.com

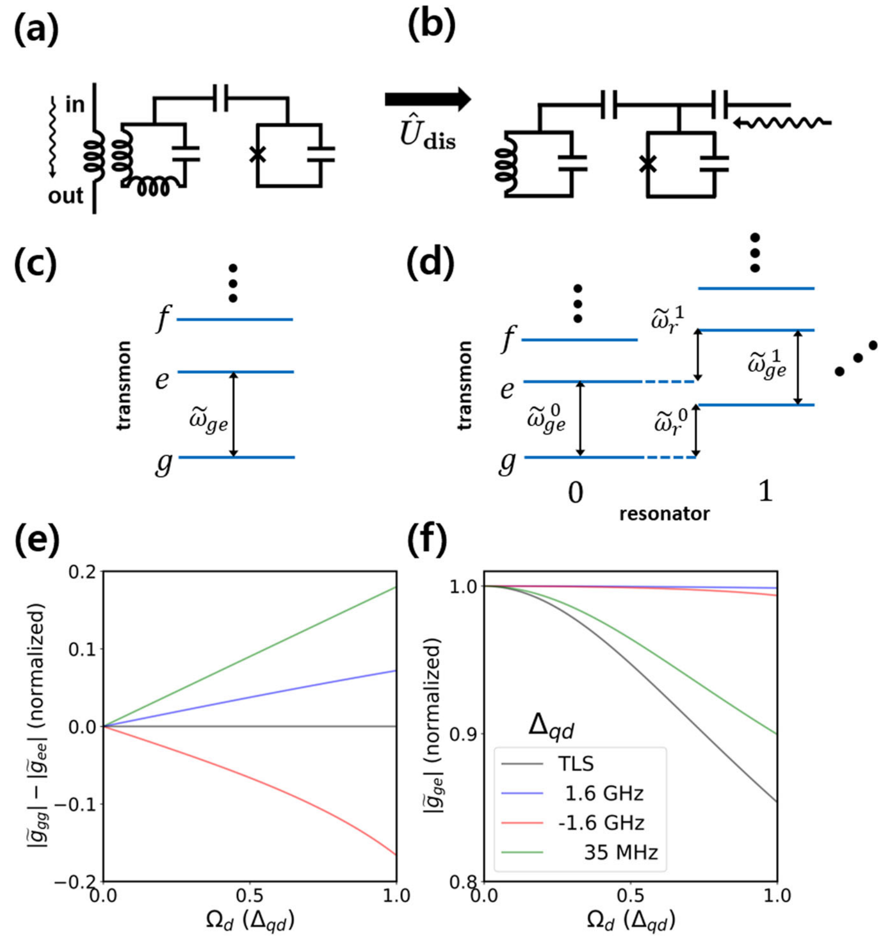

Fig. 1 | Description of drive-induced Lamb shift engineering. a Simplified diagram of circuitry. A transmon is capacitively coupled to a resonator mode. In the experiment, a drive field is inductively applied to the resonator (wavy arrow). **b** Transformed circuitry effectively identical with **a**, **c**, **d** Energy diagram of the effective static Hamiltonians $\hat K_q$ and $\hat K$. **e**, **f** Calculated renormalized coupling matrix elements $\tilde g_{ge}$, $\tilde g_{gg}$, $\tilde g_{ee}$ for several transmon-drive field detunings Δ_{qd} (red, blue, and green). For a two-state (TS) system (black), $\tilde g_{nm}$ are nearly independent of Δ_{qd}. Drive amplitudes Ω_d in x-axis is normalized by Δ_{qd}. The transmon and resonator's parameters used in the calculation are the same as the experimental values.

inductively applied to the resonator. In the lab frame, the system Hamiltonian reads

$$\hat H^{(\rm lab)} = \underbrace{4E_C(\hat N - N_g)^2 - E_J\cos\hat\phi}_{\hat H_q} + \underbrace{\omega_r\hat a^\dagger\hat a}_{\hat H_r} + \underbrace{ig\hat N(\hat a - \hat a^\dagger)}_{\hat H_I} + \underbrace{\Omega_d^{(\rm lab)}(\hat a + \hat a^\dagger)\sin\omega_d t}_{\hat H_d^{(\rm lab)}}\,. \tag{1}$$

$\hat N$, $\hat\phi$, and $\hat a$ refer to cooper-pair number, superconducting phase, and resonator field operator. E_C, E_J, and N_g are the charging, Josephson energies, and offset cooper-pair numbers of the trasmon. $\Omega_d^{(\mathbf{lab})}$ and ω_r mean the resonator drive amplitude and frequency. g is the coupling strength between the transmon and resonator.

To efficiently capture renormalization of the transmon-resonator interaction $\hat H_I$, we apply a displacement operator $\hat U^{(\mathbf{dis})} = e^{\xi(t)\hat a^\dagger - \xi^*(t)\hat a}$ on $\hat H^{(\mathbf{lab})}$. Here, $\xi(t) = \frac{i\Omega_d}{2\Delta_{rd}}e^{-i\omega_d t} - \frac{i\Omega_d}{2\Sigma_{rd}}e^{i\omega_d t}$. Δ_{rd} and Σ_{rd} are $\omega_r - \omega_d$ and $\omega_r + \omega_d$, respectively. Note that this transformation is only valid when Δ_{rd} is much larger than the linewidth of the resonator. Then, the transformed Hamiltonian reads

$$\begin{aligned}\hat H &= \hat U^{(\rm dis)}[\hat H^{(lab)} - i\partial_t]\hat U^{(\rm dis)\dagger} \\ &= \hat H_q + \hat H_I + \hat H_r + \underbrace{\Omega_d\hat N\cos\omega_d t}_{\hat H_d}\,.\end{aligned} \tag{2}$$

While eliminating $\hat H_d^{(\mathbf{lab})}$, we obtain a transmon drive $\hat H_d$, and Ω_d therein is $g(\frac{\Omega_d^{(\rm lab)}}{\Delta_{rd}} - \frac{\Omega_d^{(\rm lab)}}{\Sigma_{rd}})$. An equivalent circuit configuration is given in Fig. 1(b).

We introduce unitary transformations $\hat U_q$ and $\hat U$, which transform $\hat H_q + \hat H_d$ and $\hat H$ to effective static Hamiltonian $\hat K_q$ and $\hat K$ respectively[18]. We depict the energy levels of $\hat K_q$ and $\hat K$ in Fig. 1c, d. We define $\tilde\omega_{nm}$ the transition frequency between n-th and m-th states of $\hat K_q$. We also define $\tilde\omega_{nm}^k$ ($\tilde\omega_r^l$), which refers to the transmon (resonator) transition frequency when the resonator (transmon) is in the k-th (l-th) state. To efficiently distinguish the transmon and resonator states, we label the lowest four states of the transmon by g, e, f, and d, respectively.

The difference between $\hat K_q$ and $\hat K$ is originated from the interaction between the transmon and resonator. Particularly, the discrepancy between $\tilde\omega_{nm}^0$ and $\tilde\omega_{nm}$ can be interpreted as a transmon frequency shift when the resonator is in vacuum. Therefore, we can define renormalized Lamb shift $\tilde L_{nm} = \tilde\omega_{nm}^0 - \tilde\omega_{nm}$, and resonator frequency pulling $\tilde P = \tilde\omega_r^g - \omega_r$. All $\tilde\omega_{nm}$, $\tilde\omega_{nm}^k$, $\tilde L_{nm}$, and $\tilde P$ are adiabatically connected to ω_{nm}, ω_{nm}^k, L_{nm}, and P with $\Omega_d \to 0$. We further define AC Stark shift of the transmon $\delta\omega_{nm} = \tilde\omega_{nm} - \omega_{nm}$. We also define $\delta\omega_{nm}^k = \tilde\omega_{nm}^k - \omega_{nm}^k$. For far off-resonant drives, $\delta\omega_{nm} \approx \delta\omega_{nm}^k$ is satisfied since the interplay between AC Stark and Lamb shift is negligible.

To gain an intuition of how the transmon-resonator interaction accounts for the difference in $\tilde\omega_{nm}$ and $\tilde\omega_{nm}^0$, it is useful to define the renormalized interaction Hamiltonian[18]

$$\begin{aligned}\hat{\tilde H}_I &= ig[\hat U_q\hat N\hat U_q^\dagger](\hat a - \hat a^\dagger) \\ &\cong i\sum_{n,m}\tilde g_{nm}(e^{i(n-m+1)\omega_d t} - e^{i(n-m-1)\omega_d t})|n\rangle\langle m|(\hat a - \hat a^\dagger).\end{aligned} \tag{3}$$

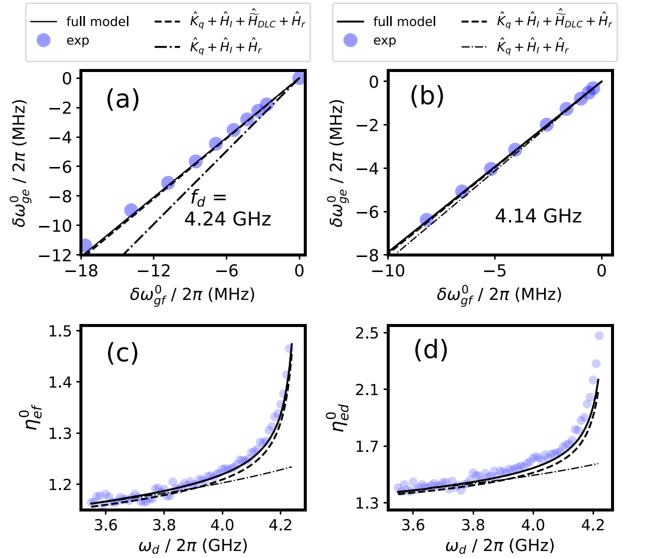

Fig. 2 | Identifying drive-induced longitudinal coupling (DLC) from multi-level spectroscopy. We investigate drive frequency ω_d near ω_r^g. Circles denote experimental data. Lines indicate theoretical calculation based on the corresponding Hamiltonian models in legend. **a**, **b** We plot the frequency shifts in *ge* transition ($\delta\omega^0_{ge}$) with respect to that of *gf* transition ($\delta\omega^0_{gf}$) for $\omega_d/2\pi = f_d = 4.24$ GHz and $\omega_d/2\pi = f_d = 4.14$ GHz, respectively. **c**, **d** We plot dimensionless quantities $\eta^0_{ef} = \frac{1}{2}\delta\omega^n_{gf}/\delta\omega^n_{ge}|_{\Omega_d\to 0}$ and $\eta^0_{ed} = \frac{1}{2}\delta\omega^n_{gd}/\delta\omega^n_{ge}|_{\Omega_d\to 0}$, while sweeping ω_d. Errors are less than the size of symbols, and thus not presented in the plots. The errors are statistical and originated when extracting $\delta\omega^0$ from data.

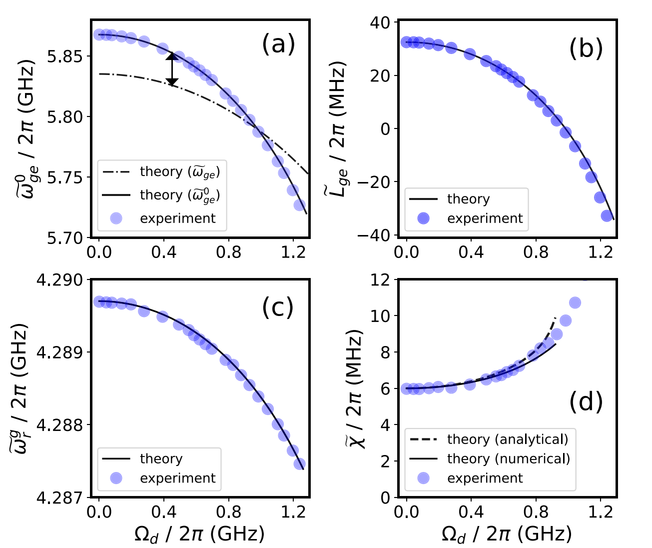

Fig. 3 | Lamb shift and other renormalized quantities with respect to drive amplitude Ω_d. Drive frequency $\omega_d/2\pi$ is 4.2 GHz for all cases. Circles and lines denote experimental data and theoretical calculation, respectively. We plot the renormalized transmon transition frequency ($\tilde{\omega}^0_{ge}$ and $\tilde{\omega}_{ge}$) in **a**, Lamb shift ($\tilde{L}_{ge}$) in **b**, resonator frequency ($\tilde{\omega}^g_r$) in **c**, and cross-nonlinearity ($\tilde{\chi}$) in **d**. Errors are less than the size of symbols, and thus not presented in the plots. Errors are statistical and originated when extracting $\delta\omega^0$ from data.

Here, $|n\rangle$ is the eigenstate of $\hat{H}_q$. For the discussion later, we define $\hat{\tilde{H}}_{\mathrm{DLC}}$, the renormalized interaction Hamiltonian containing only drive-induced longitudinal coupling (DLC)

$$\hat{\tilde{H}}_{\mathrm{DLC}} = i\sum_n \tilde{g}_{nn}(e^{i\omega_d t} - e^{-i\omega_d t})|n\rangle\langle n|(\hat{a} - \hat{a}^\dagger). \tag{4}$$

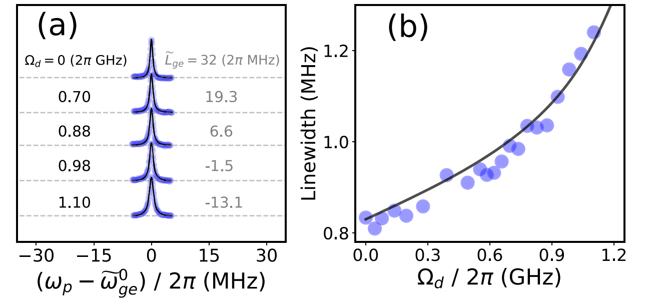

Fig. 4 | Linewidth broadening by the drive-induced dephasing. Drive frequency $\omega_d/2\pi$ is set by 4.2 GHz. **a** The transmon's two-tone spectroscopy data with respect to various Ω_d. ω_p refers to probe frequency. Corresponding renormalized Lamb shift $\tilde{L}_{ge}$ are also presented. Circles and lines denote data and Lorentzian fits. **b** Extracted linewidths with respect to Ω_d. Line is obtained by theoretical model. The linewidth broadening is originated by the finite lifetime of the resonator. Errors are less than the size of symbols, and thus not presented in the plots. The errors in **b** are statistical and originated when extracting the linewidth from **a**.

For far off-resonant drives, the magnitudes of static components ($n - m = \pm 1$) in Eq. (3) remain nearly invariant. Also, the magnitudes of off-diagonal dynamical components ($n \neq m$ and $n - m \neq \pm 1$) are much smaller compared to those of the static components. In this work, we focus on the DLC terms in Eq. (4), which in turn significantly contribute to $\tilde{L}_{nm}$.

In Fig. 1e, f, we theoretically calculate some elements of static ($\tilde{g}_{ge}$) and DLC terms ($\tilde{g}_{gg,ee}$) for several $\Delta_{qd} = \omega_{ge} - \omega_d$ and Ω_d Based on ref. 18. These mainly determine $\tilde{L}_{ge}$. The parameters used in the calculation are the same as the experimental values. In Fig. 1(e), we observe the discrepancy between $|\tilde{g}_{gg}|$ and $|\tilde{g}_{ee}|$ for both far-off-resonant (red and blue) and near-resonant (green) drive fields. For two-state (TS) systems, $|\tilde{g}_{gg}| = |\tilde{g}_{ee}|$ always holds. Figure 1f presents $|\tilde{g}_{ge}|(= |\tilde{g}_{eg}|)$. As we can confirm in Fig. 1(f), near-resonant driving significantly renormalizes $\tilde{g}_{ge}$. For far-off-resonant driving, the static components remain nearly the same. In addition, the magnitude of other off-diagonal dynamical terms are negligible (not present in Fig. 1f). Therefore, the transverse part in the renormalized interaction Hamiltonian can be approximated to $\hat{H}_I$.

Eventually, taking only the static and DLC components into consideration, we can approximate $\tilde{L}_{n,n+1}$ by

$$\tilde{L}_{n,n+1} \approx \frac{|\tilde{g}_{n,n+1}|^2}{\tilde{\omega}_{n,n+1} - \omega_r} + \frac{|\tilde{g}_{nn}|^2 - |\tilde{g}_{n+1,n+1}|^2}{\omega_d - \omega_r}. \tag{5}$$

Eq. (5) provides a rough estimation of $\tilde{L}_{n,n+1}$ when $|\tilde{g}_{n,n+1}| \ll |\tilde{\omega}_{ge} - \omega_r|$ and $|\tilde{g}_{nn}|, |\tilde{g}_{n+1,n+1}| \ll |\omega_d - \omega_r|$ are satisfied. The first term describes the Lamb shift induced by the static components in Eq. (3). The second term corresponds to the Lamb shift induced by DLC. When ω_d is closed to ω_r, the DLC-induced Lamb shift can contribute significantly to $\tilde{L}_{n,n+1}$ keeping $\tilde{g}_{n,n+1} \approx g_{n,n+1}$.

This scheme is not possible for two-state system for $|\tilde{g}_{gg}| = |\tilde{g}_{ee}|$. In Supplementary Note 2, we generalize the theoretical description in this subsection to arbitrary multi-level systems coupled to resonator modes based on Floquet formalism.

Experimental conditions

We obtain the experimental data from two cooldowns due to an accidental interruption in the experiment caused by a technical issue. The circuit parameters for each round are distinguished by unbracketed (1st) and bracketed values (2nd). The data in Fig. 2 is obtained in the first round. Figures 3 and 4 are obtained from the data in the second round. From the pulsed qubit spectroscopy, we obtain $\omega^0_{ge}/2\pi \approx 5.901(5.867)$ GHz, $\omega^0_{ef}/2\pi \approx 5.749(5.715)$ GHz, $\omega^0_{fd}/2\pi \approx 5.587(5.553)$ GHz, and $\omega^g_r/2\pi \approx 4.290(4.289)$ GHz. We also obtain $\omega_r/2\pi \approx 4.335(4.335)$ GHz by driving the transmon to unconfined states[21]. Based on these, we extract bare qubit parameters and coupling, $\omega_{ge}/2\pi \approx 5.869(5.835)$ GHz, $\omega_{ef}/2\pi \approx 5.708(5.676)$ GHz, $\omega_{fd}/2\pi \approx 5.539(5.510)$ GHz, and $g/2\pi \approx 248(245)$ MHz. The extracted parameters are consistent with the observed self and cross-nonlinearity, $A = \omega^0_{ge} - \omega^0_{ef} \approx 2\pi \times 152(150)$ MHz and $\chi = \omega^g_r - \omega^e_r \approx 2\pi \times 5.8(6.0)$ MHz, respectively. Please see Supplementary Note 1, Supplementary Table 1 and 2 for detailed information on system parameters and variables.

Resolving drive-induced longitudinal coupling

Experimentally verifying the existence of drive-induced longitudinal coupling (DLC) is non-trivial. Both DLC and AC Stark shifts yields $\delta\omega^0_{nm} \sim O(\Omega_d^2)$, and thus, one cannot distinguish them just simply measuring the changes in ω^0_{nm} without independent calibration of Ω_d. Instead, we investigate the ratios among $\delta\omega^0_{nm}$ to identify the DLC. We introduce the following dimensionless quantities.

$$\begin{aligned} \eta^n_{ef} &= \tfrac{1}{2}\,\delta\omega^n_{gf}/\delta\omega^n_{ge}|_{\Omega_d \to 0}, \\ \eta^n_{ed} &= \tfrac{1}{3}\,\delta\omega^n_{gd}/\delta\omega^n_{ge}|_{\Omega_d \to 0}. \end{aligned} \tag{6}$$

We will compare experimentally obtained η to the theory with and without considering DLC, and thereby verify the effects of the DLC. Note that finding experimental η does not demand calibrating Ω_d since it is independent of Ω_d.

In Fig. 2, we measure both η^0_{ef} and η^0_{ed} from multi-level spectroscopy[22]. Please see Supplementary Note 3 for details on the experimental methods. In Fig. 2a, b, we present the observed $\delta\omega^0_{ge}$ with respect to $\delta\omega^0_{gf}$ (circles) for two different drive frequencies near ω^g_r, 4.24 GHz (a) and 4.14 GHz (b), respectively. We choose ω_d to be close enough to ω_r since the effects of the DLC scale linearly with $1/(\omega_d - \omega_r)$ as shown in Eq. (5). We confirm linear correlations among experimentally observed $\delta\omega^0_{ge,gf,gd}$ for $\delta\omega^0_{ge,gf,gd}/2\pi \lesssim 10$MHz as seen in Fig. 2a, b. In Fig. 2c, d, we sweep ω_d from 3.55 GHz to 4.25 GHz and present corresponding η^0_{ef} and η^0_{ed} from the experiments (circles).

The solid, single-dashed, and dot-dashed lines refer to the theoretical calculations based on $\hat{K}_q + \widetilde{H}_I + \hat{H}_r$, $\hat{K}_q + \hat{H}_I + \widetilde{H}_{\mathrm{DLC}} + \hat{H}_r$, and $\hat{K}_q + \hat{H}_I + \hat{H}_r$, respectively. We apply Floquet theory[23,24] to the above Hamiltonians and calculate the theoretical values. The calculations are numerically done by QuTip[25,26].

The first model presents a full description of the driven system, which excellently explains the experimental data. The second and third models differs only by a term $\widetilde{H}_{\mathrm{DLC}}$. Therefore, the disagreements between these models can be interpreted as the effects from the DLC. The breakdown of the dot-dashed lines in Fig. 2a–d, and the excellent consistency among the experiment, the solid and single-dashed lines indicate clear evidences for the DLC. As expected from Eq. (5), we can confirm that the DLC effect is larger with smaller $|\omega_d - \omega_r|$ in Fig. 2a, b. Such tendency is also clearly confirmed in Fig. 2c, d.

From the investigation of this section, we conclude that calibrating Ω_d cannot be precisely achieved only using AC Stark shift theory since the DLC should take a significant portion of the frequency shifts. In the following section, we use a more rigorous approach to find Ω_d, and thereby extract the Lamb shifts at arbitrary drives.

Lamb shift renormalization at arbitrary drive strengths

In the previous section, we have proven the existence of DLC effects, and thereby learned employing AC Stark shift theory alone is an inappropriate approach to calibrate Ω_d. From now on, we use Eq. (2), including the resonator and interaction terms, to obtain Ω_d in the experiment. We then quantify the renormalized Lamb shift at arbitrary Ω_d. We cross-check our quantification from the shifts in the resonator frequency and cross-nonlinearity. Note that the AC Stark shift alone cannot explain these shifts simultaneously.

Figure 3 present experimentally observed $\widetilde{\omega}^0_{ge}$, $\widetilde{\omega}^g_r$, and $\widetilde{\chi}$ (circles) for $\omega_d/2\pi = 4.2$ GHz. We first obtain the conversion factor $\mu(\omega_d)$ that satisfies $\mu(\omega_d)\sqrt{P_d} = \Omega_d$, where P_d indicates the driving power measured at the signal generator. We set $\mu = 138.9$, with which all quantities are simultaneously explained by the theories.

In Fig. 3a, we compare experimentally observed $\widetilde{\omega}^0_{ge}$ to theoretical expectation (solid line). For a comparison, we plot the $\widetilde{\omega}_{ge}$ (dot-dashed line) theoretically calculated based on $\hat{K}_q$. An arrow indicates $\widetilde{L}_{ge} = \widetilde{\omega}^0_{ge} - \widetilde{\omega}_{ge}$. There is a crossing between the data and dot-dashed line, which means the sign of $\widetilde{L}_{ge}$ is flipped at that drive amplitude. In Fig. 3b, c, we plot experimentally observed $\widetilde{L}_{ge}$ and $\widetilde{\omega}^g_r$ with the theoretical expectation (lines). $\widetilde{L}_{ge}$ varies from 32 to -30 MHz. The changes in the resonator frequency pulling $\widetilde{P} = \widetilde{\omega}^g_r - \omega_r$ is relatively less than those of $\widetilde{L}_{ge}$. All the theoretical calculations in (a-c) are based on Floquet theory and numerically performed by QuTip[25,26].

We present the renormalized cross-nonlinearities ($\widetilde{\chi}$) of the driven transmon-resonator system in Fig. 3(d). The circles and lines indicate the experimental and theoretical calculation, respectively. We investigate the origin of Ω_d dependence of $\widetilde{\chi}$. In the analytical theory (dashed line), we use the perturbative calculation $\widetilde{\chi} \approx \widetilde{g}^2_{ge}\widetilde{A}/(\widetilde{\omega}^0_{ge} - \widetilde{\omega}^0_r - \widetilde{A})$[20], and use the approximation $\widetilde{g}_{ge} \approx g_{ge}$. Here, $\widetilde{A}$ is the renormalized self-nonlinearity, $\widetilde{\omega}^0_{ge} - \widetilde{\omega}^0_{ef}$. We do not make any approximation on $\widetilde{A}$ in the analytical calculation. The analytical theory is consistent with the experimental data as well as the numerical calculation based on Floquet theory (solid line). Therefore, we can conclude that the approximation $\widetilde{g}_{ge} \approx g_{ge}$ is satisfied. The disagreement between solid and dashed lines at large Ω_d in Fig. 3d can be attributed to undesired sideband transitions between the transmon and resonator. See Supplementary Note 3 for more detailed discussion.

Drive-induced dephasing

In Fig. 4, we investigate how the transmon's linewidth varies while engineering $\widetilde{L}_{ge}$ from 32 to -30 MHz. Figure 4a shows two-tone spectroscopy of $g \to e$ transition for various Ω_d. Corresponding $\widetilde{L}_{ge}$ is also presented beside. We obtain $\Gamma^q_1 \approx 1$ MHz and $\Gamma^q_\phi \approx 2$ MHz from time-domain measurement, where Γ^q_1 and Γ^q_ϕ are energy relaxation and pure dephasing rates of the transmon. Corresponding linewidth in two-tone spectroscopy is approximately 830 kHz without probe power broadening and measurement-induced dephasing[27,28]. We also obtain the similar linewidth from two-tone spectroscopy in the experiment, when the calibrated pump strength is approximately 110 kHz, and measurement photon number is far less than unity. There are almost no qualitative changes in the spectrum presented in Fig. 4a with increasing Ω_d. However, we notice the linewidth increases by a significant amount. Figure 4b shows the extracted linewidth from Lorentzian fitting (circles). We name such effect drive-induced dephasing (DID) in this paper.

We reveal that the cooperative effects from the driving and finite resonator lifetime can explain the linewidth broadening. The amount of DID is defined by $\Gamma^q_{\phi,\mathrm{DID}}$. The same phenomenon is also theoretically predicted in[29], but has been rarely demonstrated experimentally. Based on Eq.33 of[29], we obtain the approximated form of $\Gamma^q_{\phi,\mathrm{DID}}$

$$\Gamma^q_{\phi,\mathrm{DID}} \approx \frac{\sqrt{\widetilde{A}\widetilde{\chi}}}{2\widetilde{\Delta}_{rd}} \frac{\Omega_d}{2\widetilde{\Delta}_{qd}} \times \Gamma^r_1(\omega_d). \tag{7}$$

$\widetilde{\Delta}_{qd}$ and $\widetilde{\Delta}_{rd}$ are given by $\widetilde{\omega}^0_{ge} - \omega_d$ and $\widetilde{\omega}^g_r - \omega_d$, respectively. $\Gamma^r_1(\omega)$ is the resonator-bath coupling. We have $\Gamma^r_1(\omega^g_r) = 13.47$ MHz from the resonator decay rate, which is mainly accounted for by the external coupling to the feedline. The theory curve in Fig. 4(b) is based on Eq. (7). $\Gamma^r_1(\omega_d)$ is determined by some unknown factors such as the cable resonances of feedlines, and empirically known slowly varying over a few hundreds MHz frequency scale. Thus, we set $\Gamma^r_1(\omega_d)$ as a free-fitting parameter and obtain the value of $(0.83 \pm 0.05) \times \Gamma^r_1(\omega^g_r)$ from the least chi-square method. See also extended data in Supplementary Note 5, Supplementary Figs. 6 and 7.

If we directly drive the transmon using a separate charge-line, instead indirectly drive through the resonator, the DID can be suppressed approximately by a factor of g/Δ_{qr}[29]. For the system in the dispersive coupling regime, $g/\Delta_{gr} \ll 1$ is satisfied. Hence, the DID can be significantly reduced. Since $\Gamma^{q}_{\phi,\mathrm{DID}}$ scale linearly with $\Gamma^{r}_{1}(\omega_d)$, the DID becomes negligible for high-coherence resonators when $\Gamma^{r}_{1}(\omega)$ is negligible around $\omega \sim \omega_d$. For readout resonators that need sufficient external couplings to the feedlines for high readout efficiencies, one can engineer the interface between resonators and feedlines suppressing $\Gamma^{r}_{1}(\omega_d)$ while keep large enough $\Gamma^{r}_{1}(\omega^{g}_{r})$, as a similar strategy is used for Purcell filters.

The magnitude of the DID when we tune the Lamb shift to zero is approximately 1 MHz. We can suppress this to 1 kHz with $g/\Delta_{gr} = 0.1$ and $\Gamma^{r}_{1}(\omega_d) = 10$ kHz, which are achievable values in typical circuit QED experiments. Nonetheless, it is undeniable that the suggested measures do not thoroughly eliminate the DID and complicate the circuit design. Therefore, our scheme might not be practical when a superconducting qubit of extremely low pure dephasing rate less than 1 kHz is required. However, our approach is still available for the other applications where moderate coherence times are acceptable[30–34].

Conclusion

To summarize, we experimentally realize a large tuning of the Lamb shift ~30 MHz with drive strength while minimizing undesired renormalization of the other properties of the transmon-resonator system. We show that the Lamb shift can be engineered even to zero. Our observation is consistent with multi-level transmon spectroscopy as well as other renormalized quantities such as cross-nonlinearities and resonator frequency pulling. The observation also agrees excellently with Floquet theory.

Controlling the Lamb shift could provide more flexibilities in engineering the transition frequencies of superconducting qubits. The feasibility of tuning the Lamb shift to zero possesses other practical implications. Our approach can also be implemented to multi-qubit device without substantial complexities. We provide specific application examples using the above merits in Supplementary Note 4.

Methods

Eigenenergy calculation

In this work, we utilize QuTiP to apply Floquet theory to the driven Hamiltonian models presented in the main text. Our goal is to find the quasi-eigenenergies of the driven Hamiltonians ($\widetilde{E}_{n,\alpha_n}$) that are adiabatically connected to the eigenenergies of the undriven Hamiltonians (E_n) when the drive amplitudes are turned off ($\Omega_d \to 0$). We use the 'floquet modes' method of QuTiP, which returns the quasi-eigenenergies in the first Floquet Brillouin zone of the given Hamiltonian, i.e., $\widetilde{E}_{n,0}$ for all n. However, these values are not sequentially arranged with respect to n, and the sequence even changes as Ω_d varies. Therefore, we need to take additional steps to find the proper Floquet mode number α_n and quasi-eigenenergies. We gradually increase Ω_d with a sufficiently small step size and, at every step, find the proper $\widetilde{E}_{n,0}$ and corresponding α_n such that they are adiabatically connected to the values obtained in the previous step. At the beginning, when $\Omega_d = 0$ is satisfied, we can find E_n using the 'eigenenergies' method without Floquet theory, and therefore finding the proper mode numbers is unnecessary. We properly adjust the step size when increasing Ω_d to balance accuracy and computation time.

Device fabrication and measurement

The device and cryogenic setup used in this work are identical to those in our previous work[18]. The device consists of a transmon coupled to two coplanar waveguide resonators, but only one of the resonators is used in this work because the other one is weakly coupled with a cross-nonlinearity of less than 100 kHz, and therefore not effective in the experiments. The transmon and resonators are defined on a 100 nm niobium titanium nitride (NbTiN) film on a 525 μm thick silicon substrate[35]. The Al-AlOx-Al Josephson junction of the transmon is fabricated by typical double-angle shadow evaporation. The device is mounted on the mixing chamber plate of a dilution fridge (LD-400) and shielded from radiation and magnetic field using Cooper and Aluminum cans. The optical microscope image of the device is presented in[18].

Data availability

Data supporting the plots within the main text of this paper are available through Zenodo at https://doi.org/10.5281/zenodo.7847837. Further information is available from the corresponding author upon reasonable request.

Code availability

Code used to produce the plots within this paper is available from the corresponding author upon reasonable request.

Received: 6 May 2024; Accepted: 17 October 2024;
Published online: 25 October 2024

References

1. Lamb Jr, W. E. & Retherford, R. C. Fine structure of the hydrogen atom by a microwave method. *Phys. Rev.* **72**, 241 (1947).
2. Heinzen, D. J. & Feld, M. S. Vacuum radiative level shift and spontaneous-emission linewidth of an atom in an optical resonator. *Phys. Rev. Lett.* **59**, 2623 (1987).
3. Haroche, S., Brune, M. & Raimond, J. M. Cavity to circuit quantum electrodynamics. *Nat. Phys* **16**, 243 (2020).
4. Blais, A., Grimson, A., Girvin, S. M. & Wallraf, A. Circuit quantum electrodynamics. *Rev. Mod. Phys.* **93**, 025005 (2021).
5. Blais, A. et al. Quantum-information processing with circuit quantum electrodynamics. *Phys. Rev. A* **75**, 032329 (2007).
6. Franger, A. et al. Resolving vacuum fluctuations in an electrical circuit by measuring the lamb shift. *Science* **322**, 1357 (2008).
7. Ao, Z. et al. Extremely large lamb shift in a deep-strongly coupled circuit QED system with a multimode resonator. *Sci. Rep.* **13**, 11340 (2023).
8. Mirhosseini, M. et al. Superconducting metamaterials for waveguide quantum electrodynamics. *Nat. Comm* **9**, 3706 (2018).
9. Léger, S. et al. Observation of quantum many-body effects due to zero point fluctuations in superconducting circuits. *Nat. Comm* **10**, 5259 (2019).
10. Malekakhlagh, M., Petrescu, A. & Türeci, H. E. Cutoff-free circuit quantum electrodynamics. *Phys. Rev. Lett.* **119**, 073601 (2017).
11. Gely, M. F. et al. Convergence of the multimode quantum Rabi model of circuit quantum electrodynamics. *Phys. Rev. B* **95**, 245115 (2017).
12. Gely, M. F., Steele, G. A. & Bothner, D. The nature of the Lamb shift in weakly-anharmonic atoms: from normal mode splitting to quantum fluctuations. *Phys. Rev. A* **98**, 053808 (2018).
13. Silveri, M. et al. Broadband Lamb shift in an engineered quantum system. *Nat. Phys* **15**, 533 (2019).
14. Wen, P. Y. et al. Large collective lamb shift of two distant superconducting artificial atoms. *Phys. Rev. Lett.* **123**, 233602 (2019).
15. Yang, S., Zheng, H., Hong, R., Zhu, S. & Zubairy, M. S. Control of the Lamb shift by a driving field. *Phys. Rev. A* **81**, 052501 (2010).
16. Jentschura, U. D., Evers, J., Haas, M. & Keitel, C. H. Lamb-shift of laser-dressed atomic states. *Phys. Rev. Lett.* **91**, 253601 (2003).
17. Gramich, V., Gasparinetti, S., Solinas, P. & Ankerhold, J. Lamb-shift enhancement and detection in strongly driven superconducting circuits. *Phys. Rev. Lett.* **113**, 027001 (2014).
18. Ann, B., Deve, S. & Steele, G. A. Resolving nonperturbative renormalization of a microwave-dressed weakly anharmonic superconducting qubit coupled to a single quantized mode. *Phys. Rev. Lett.* **131**, 193605 (2023).
19. Wu, L.-A. & Lidar, D. A. Dressed qubits. *Phys. Rev. Lett.* **91**, 097904 (2003).
20. Koch, J. et al. Charge-insensitive qubit design derived from the cooper pair box. *Phys. Rev. A* **76**, 042319 (2007).
21. Lescanne, R. et al. Escape of a driven quantum josephson circuit into unconfined states. *Phys. Rev. Appl.* **11**, 014030 (2019).
22. Schneider, A. et al. Local sensing with the multilevel ac Stark effect. *Phys. Rev. A* **97**, 062334 (2018).

23. Shirley, J. H. Solution of the Schrödinger Equation with a Hamiltonian periodic in time. *Phys. Rev.* **B97**, 138 (1965).
24. Sambe, H. Steady states and quasienergies of a quantum-mechanical system in an oscillating field. *Phys. Rev. A* **7**, 2203 (1973).
25. Johansson, J. R., Nation, P. D. & Nori, F. QuTiP: An open-source Python framework for the dynamics of open quantum systems. *Comp. Phys. Comm.* **183**, 1760 (2012).
26. Johansson, J. R., Nation, P. D. & Nori, F. QuTiP 2: A Python framework for the dynamics of open quantum systems. *Comp. Phys. Comm.* **184**, 1234 (2013).
27. Gambetta, J. et al. Qubit-photon interactions in a cavity: Measurement-induced dephasing and number splitting. *Phys. Rev. A* **74**, 042318 (2006).
28. Schuster, D. I. et al. ac stark shift and dephasing of a superconducting qubit strongly coupled to a cavity field. *Phys. Rev. Lett.* **94**, 123602 (2005).
29. Petrescu, A., Malekakhlagh, M. & Türeci, H. E. Lifetime renormalization of driven weakly anharmonic superconducting qubits. II. The readout problem. *Phys. Rev. B* **129**, 134510 (2020).
30. Clerk, A. A., Lehnert, K. W., Bertet, P., Petta, J. R. & Nakamura, Y. Hybrid quantum systems with circuit quantum electrodynamics. *Nat. Phys* **16**, 257 (2020).
31. Kristen, M. et al. Amplitude and frequency sensing of microwave fields with a superconducting transmon qudit. *npj Quantum Inf.* **6**, 57 (2020).
32. Hönigl-Decrinis, T., Shaikhaidarov, R., De Graaf, S. E., Antonov, V. N. & Astafiev, O. V. Two-level system as a quantum sensor for absolute calibration of power. *Phys. Rev. Appl.* **13**, 024066 (2020).
33. Preskill, J. Quantum computing in the NISQ era and beyond. *Quantum* **2**, 79 (2018).
34. Sagastizabal, R. E. *Experimental Quantum Simulation with noisy intermediate-scale superconducting processors* Dissertation, Delft University of Technology (2023).
35. Thoen, D. J. et al. Superconducting NbTiN Thin Films with Highly Uniform Properties Over a ø 100 mm Wafer, *IEEE Trans. Appl. Superconduct.*, **27**, 1500505 (2017).

Acknowledgements

We thank David Thoen and Jochem Baselmans for providing us with NbTiN films. Byoung-moo Ann acknowledges support from the European Union's Horizon 2020 research and innovation program under the Marie Sklodowska-Curie grant agreement No. 722923 (OMT). This work was supported by the National Research Foundation of Korea(NRF) grant funded by the Korea government(MSIT)(RS-2023-00213037). This work was also supported by Korea Research Institute of Standards and Science (KRISS-GP2024-0013-06).

Author contributions

B.A. conceived the study, made the theoretical description, and fabricated the device. B.A. also performed the numerical and experimental study. The measurement infrastructure is constructed by G.A.S. B.A. and G.A.S analyzed data. B.A. wrote the manuscript with input from G.A.S.

Competing interests

The authors declare no competing interests.

Additional information

Supplementary information The online version contains supplementary material available at https://doi.org/10.1038/s42005-024-01841-0.

Correspondence and requests for materials should be addressed to Byoung-moo Ann.

Peer review information *Communications Physics* thanks the anonymous reviewers for their contribution to the peer review of this work. A peer review file is available.